



Article

High-Accuracy Neural Network Interatomic Potential for Silicon Nitride

Hui Xu ¹ , Zeyuan Li ², Zhaofu Zhang ¹, Sheng Liu ¹, Shengnan Shen ^{1,*} and Yuzheng Guo ^{3,*}¹ The Institute of Technological Sciences, Wuhan University, Wuhan 430072, China² School of Power and Mechanical Engineering, Wuhan University, Wuhan 430072, China³ School of Electrical and Automation, Wuhan University, Wuhan 430072, China

* Correspondence: shen_shengnan@whu.edu.cn (S.S.); yguo@whu.edu.cn (Y.G.)

Abstract: In the field of machine learning (ML) and data science, it is meaningful to use the advantages of ML to create reliable interatomic potentials. Deep potential molecular dynamics (DEEPM) are one of the most useful methods to create interatomic potentials. Among ceramic materials, amorphous silicon nitride (SiN_x) features good electrical insulation, abrasion resistance, and mechanical strength, which is widely applied in industries. In our work, a neural network potential (NNP) for SiN_x was created based on DEEPM, and the NNP is confirmed to be applicable to the SiN_x model. The tensile tests were simulated to compare the mechanical properties of SiN_x with different compositions based on the molecular dynamic method coupled with NNP. Among these SiN_x , Si_3N_4 has the largest elastic modulus (E) and yield stress (σ_s), showing the desired mechanical strength owing to the largest coordination numbers (CN) and radial distribution function (RDF). The RDFs and CNs decrease with the increase of x ; meanwhile, E and σ_s of SiN_x decrease when the proportion of Si increases. It can be concluded that the ratio of nitrogen to silicon can reflect the RDFs and CNs in micro level and macro mechanical properties of SiN_x to a large extent.

Keywords: molecular dynamics; machine learning; amorphous silicon nitride; density functional theory; deep potential



Citation: Xu, H.; Li, Z.; Zhang, Z.; Liu, S.; Shen, S.; Guo, Y. High-Accuracy Neural Network Interatomic Potential for Silicon Nitride. *Nanomaterials* **2023**, *13*, 1352. <https://doi.org/10.3390/nano13081352>

Academic Editors: Frederik Tielens and Gregory M. Odegard

Received: 14 March 2023

Revised: 6 April 2023

Accepted: 9 April 2023

Published: 13 April 2023



Copyright: © 2023 by the authors. Licensee MDPI, Basel, Switzerland. This article is an open access article distributed under the terms and conditions of the Creative Commons Attribution (CC BY) license (<https://creativecommons.org/licenses/by/4.0/>).

1. Introduction

Molecular dynamics (MD) mainly rely on Newtonian mechanics to simulate the motion of molecular systems. Compared with the expensive cost of the experiment, the MD method is a cost-effective and efficient tool for exploring the properties of various complicated new materials. To make sure the simulation results match well with the experiments, it is important to use an accurate description of interatomic interactions. Quantum mechanics (QM) simulations, such as the ab initio molecular dynamics (AIMD) method based on the density functional theory (DFT), are the most reliable way to describe the atomic interactions for different systems [1–5]. Although AIMD exhibits desirable computational accuracy, the time cost of AIMD is very high, which limits the application of AIMD. To balance the calculation performance and speed of MD simulations, empirical interatomic potentials have been applied to MD simulations. Empirical interatomic potentials, including Lennard–Jones (LJ) [6], embedded atom method (EAM) [7,8], the Stillinger–Weber (SW) [9,10], Tersoff [11] and charge-optimized many-body (COMB) [12] potentials obviously improved the calculation performance and speed of MD. However, the application of these empirical potentials is hindered by their poor transferability. In terms of systems described by two-body interactions, the LJ potential has favorable accuracy. The SW and Tersoff potentials are able to combine two-body and three-body interactions to stabilize tetrahedral solids, but the description accuracy of bond breaking and metallic phases of silicon and carbon is not sufficient. Owing to the rapid development of machine learning (ML) and data science, it is meaningful to take the advantages of ML to create reliable ML interatomic potentials to replace the conventional empirical potentials [13–15]. In 2007,

J. Behler and M. Parrinello first proposed a method to create ML interatomic potentials based on artificial neural network deep learning [16]. Various ML potentials have been generated and further applied to material property calculations. Among these ML potential training methods, deep potential molecular dynamics (DEEPM) is one of the most useful methods to create interatomic potentials recently [16,17]. Results prove that the various systems that used DEEPM methods delivered good accuracy [18,19]. For example, Wang et al. developed a DEEPM potential to describe the properties of Li-Si alloys [20]. The DEEPM potential is about 20 times faster than the AIMD simulations. Meanwhile, the accuracy of DEEPM potential is comparable with that of AIMD.

Amorphous silicon nitride (SiN_x) has been widely used in advanced semiconductor packaging owing to its good electrical insulation, abrasion resistance, and mechanical strength [21–23].

However, compared to the plenty of experimental studies about SiN_x , there is less research about SiN_x on theoretical calculations at present [24–26]. In this work, we conducted a preliminary and comprehensive theoretical calculation of SiN_x . At the same time, considering that current classic MD potentials are not suitable for SiN_x simulations due to efficiency and accuracy [27–32], it is of great interest to train a new potential to describe the interatomic interactions.

In our work, a neural network potential (NNP) was trained based on the ML in the DEEPM package for SiN_x with the 3:4 composition, owing to its high stability. To validate the accuracy of the NNP, the energies and forces obtained by the NNP were compared with its AIMD counterpart. The structure and properties of Si_3N_4 calculated by MD + NNP were compared with the AIMD through the radial distribution functions (RDFs), coordination numbers (CNs), and bond angle distributions (BADs). Similar to the empirical potentials, the NNP trained by DEEPM can also be used for SiN_x with different compositions. Therefore, the NNP was confirmed to be reliable and applicable for SiN_x . In the following parts, SiN_x all refers to the amorphous silicon nitride with different compositions. Then, the NNP was applied to MD simulations to predict the properties of SiN_x . To further investigate the influence of compositions on the mechanical properties of SiN_x , the tensile tests of SiN_x were carried out at 300 K. Among these SiN_x models, the Si_3N_4 has the desired mechanical strength, which is consistent with the microstructure, including the maximal RDF peak and CNs.

2. Materials and Methods

DEEPM is one of the most popular methods to create interatomic potentials recently owing to its calculation speed and accuracy [17,33]. The details of the NNP training process are listed as follows.

2.1. AIMD Calculations

In our work, Si_3N_4 was chosen as an example to train the NNP because of the high stability of the 3:4 composition. The training database of Si_3N_4 at different temperatures was obtained by first-principles calculations using the Vienna ab initio simulation package (VASP) [34]. The exchange–correlation interaction was described by Perdew–Burke–Ernzerhof (PBE) functional [35]. The interaction between electrons and ions was described by the projector-augmented wave (PAW) approach. The cut-off energy is 520 eV. We use the k-point mesh grid with a spacing of 0.4 Å within the Gamma-centered k-sampling to sample the Brillouin zone. The initial Si_3N_4 configuration with 112 atoms is a cube with randomly distributed atoms; the model was built by LAMMPS “create_atoms” command and modified by Material Studio. The periodic boundary conditions were applied in x , y , and z directions. The cube size in the x , y , and z directions is 11.935 Å, 11.935 Å, and 11.55 Å, respectively. The AIMD calculations were fulfilled at a constant temperature of 2000 K with an NVT ensemble. The Nose-Hoover thermostat was used to control the temperature of the AIMD simulation. The timestep is 1 fs running 10,000 steps. The energy and force errors less than 10^{-5} eV/atom and 0.01 eV/Å, respectively, are convergence criteria for geometry optimization.

2.2. Deep Potential Training Process

Based on the AIMD calculations, 10,000 data points were transferred from the output file "OUTCAR"; the data points were divided into five sets. The four sets were used for training databases, with the remaining one selected as a testing database. The smooth edition of the DEEPM and DeepPot-SE model, implemented in the DEEPM-kit package [33], was used to train the interatomic potential. The cutoff radius of the model is 6.0 Å for neighbor searching with the smoothing function starting from 5.8 Å. The hidden layers were divided into three layers, and the number of neurons in each layer is 25, 50, and 100, respectively. The learning rate starts from 0.001 using a decay rate of 0.95 every 5000 steps. The decay step and stop learning rate are 5000 and 3.51×10^{-8} , respectively. Based on the datasets of AIMD calculations at 2000 K, the NNP potential at 2000 K was obtained. In order to obtain a high-quality potential, a training database including different temperatures is crucial; as a result, the same method was used for the 3000 K potential training as well. Then, the 2000 K and 3000 K NNP potentials were combined to achieve a new NNP. Finally, the NNP was frozen, and the frozen model can be used in model testing and MD simulations.

3. Results and Discussions

3.1. The Accuracy of NNP

To verify the accuracy of NNP at 2000 K and 3000 K, the energies and forces from NNP after DEEPM training were compared with those from AIMD shown in Figures 1 and 2. The results show that the validation data generally distribute around the $y = x$ line, showing that the obtained potential can predict the energies and forces precisely. The root-mean-square errors (RMSEs) and R-Square (R^2) of energies were calculated to evaluate the performance of NNP. The smaller RMSEs mean better prediction. On the contrary, the higher R^2 , between 0 and 1, indicates better results. It can be seen that the NNP with larger R^2 and smaller RMSE at y and z directions, respectively, works better than that of the x direction, both in Figures 1 and 2. Meanwhile, the R^2 and RMSE are acceptable for NNP at x direction as well.

To further validate the reliability of NNP, the RDFs, CNs, and BADs of Si_3N_4 calculated by NNP were compared with those of AIMD. To research these properties of Si_3N_4 , a simulation at 2000 K was conducted by a large-scale atomic/molecular massively parallel simulator (LAMMPS) [36] with the MD [37]. The detailed simulation parameters are shown in the Supplementary Material. The RDFs, also known as pair correlation function, usually refer to the distribution probability of other particles in the Δr thickness shell at the distance r of a specified particle. RDFs are widely used to study the degree of order of materials and describe the correlation of atoms, which can be calculated by

$$g_{\alpha\beta}(r) = \frac{V}{N_{\alpha}N_{\beta}} \sum_{\alpha} \frac{\langle N_{\alpha\beta}(r, \Delta r) \rangle}{4\pi r^2} \quad (1)$$

where V is the volume of the simulation cell. N_{α} and N_{β} are the number of α -type ions and β -type ions, respectively. $N_{\alpha\beta}(r, \Delta r)$ is the average number of α -type ions around β -type ions in a spherical space. The results of the NNP + MD and AIMD simulations in Figure 3a confirm the accuracy of the NNP. The MD in the following content is specified as MD coupled with NNP. It can be seen that the first peak values of Si_3N_4 RDFs calculated by MD are located around $r = 1.7$ Å. The results show that the distribution function $g(r)$ obtained by MD is consistent with the AIMD results calculated by VASP. The same conclusion can be reached at 3000 K in Figure 4a. Therefore, it is concluded that the NNP is capable of predicting structure information of SiN_x with AIMD accuracy within this range from 2000 K to 3000 K.

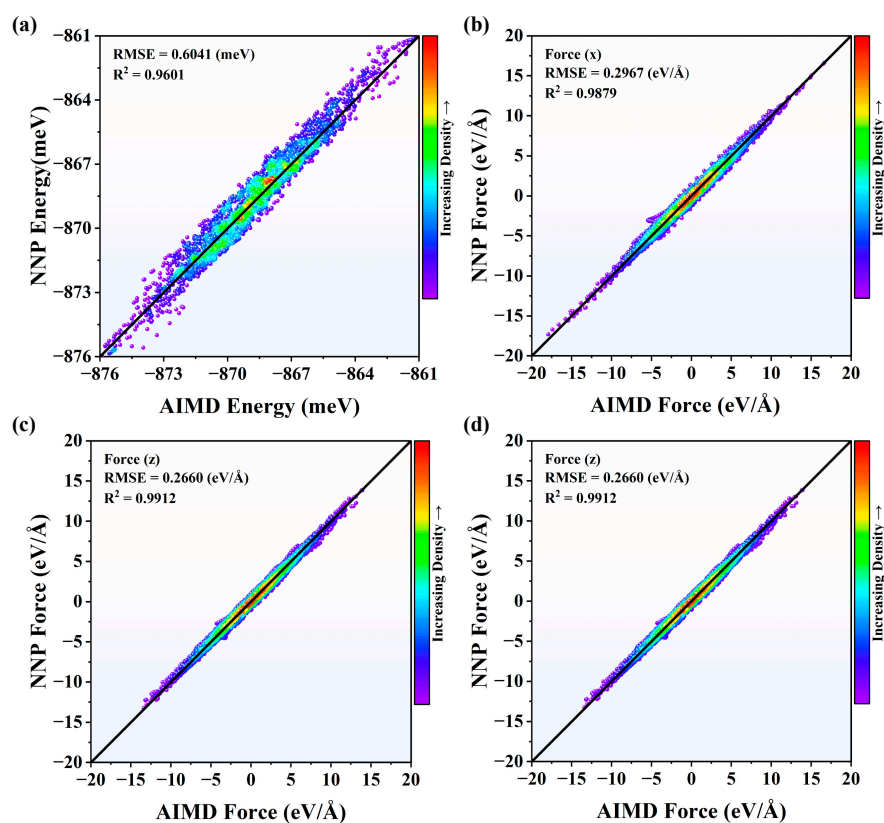


Figure 1. The comparisons of (a) energies and (b–d) forces from NNP and AIMD for Si_3N_4 at 2000 K in x , y , and z directions.

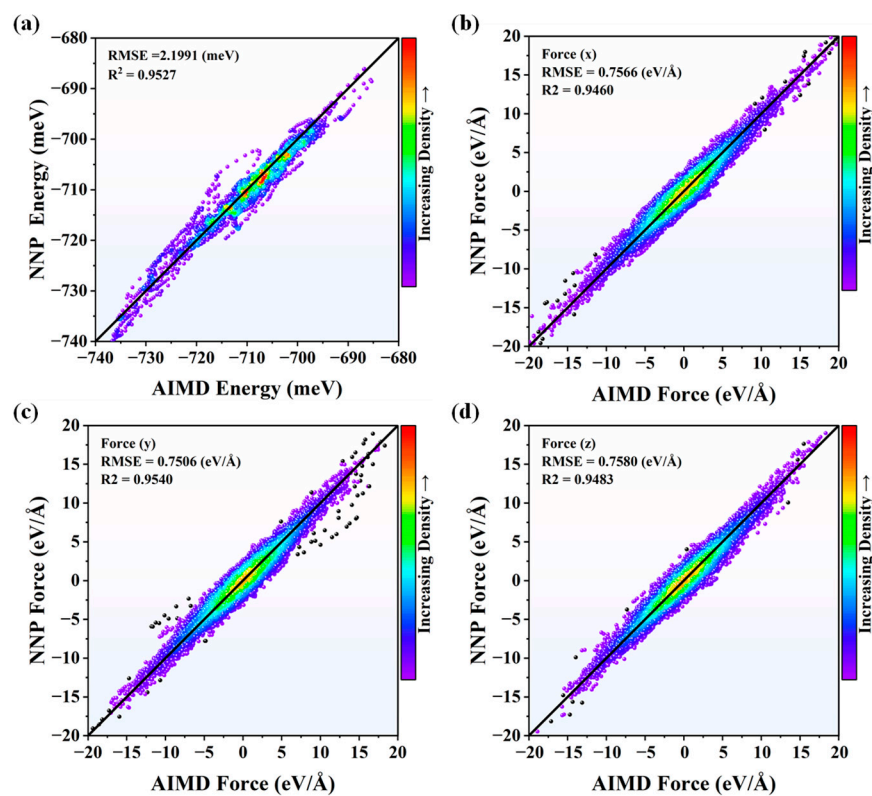


Figure 2. The comparisons of (a) energies and (b–d) forces from NNP and AIMD for Si_3N_4 at 3000 K in x , y , and z directions.

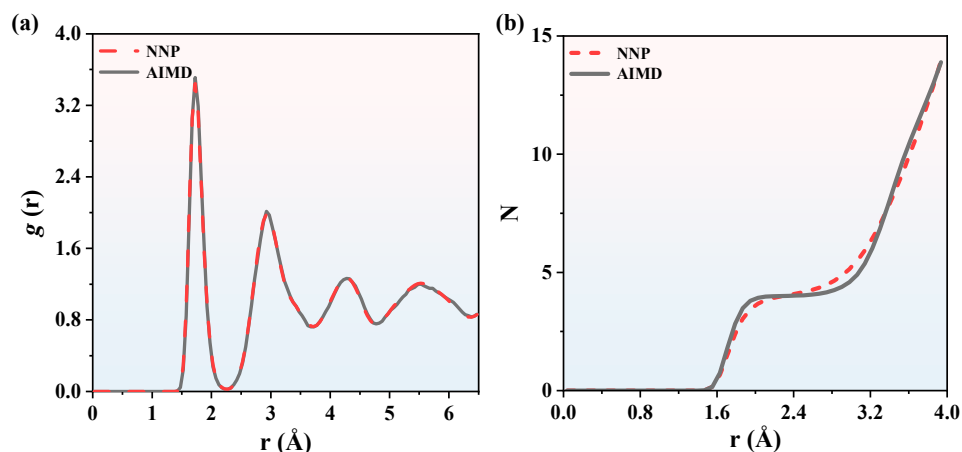


Figure 3. The comparisons of (a) Si_3N_4 RDFs between NNP + MD and AIMD calculations and (b) Si_3N_4 CNs between NNP + MD and AIMD calculations. The temperature is 2000 K.

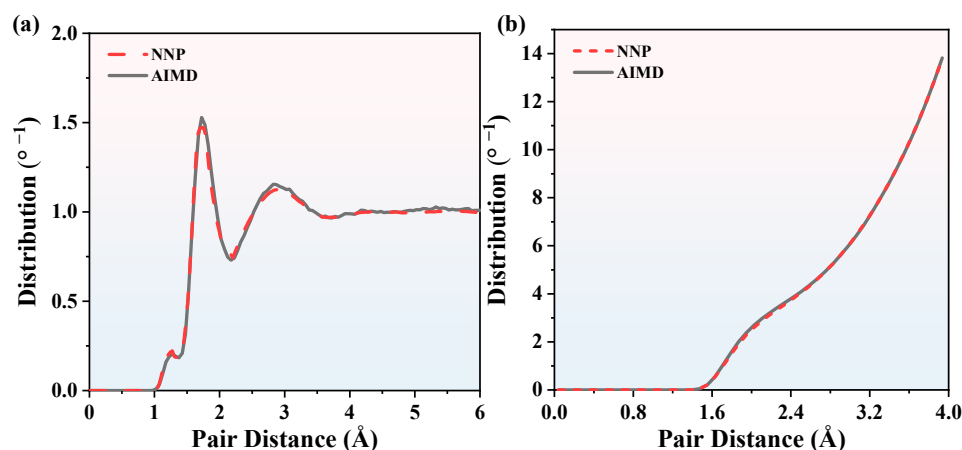


Figure 4. The comparisons of (a) Si_3N_4 RDFs between NNP + MD and AIMD calculations and (b) Si_3N_4 CNs between NNP + MD and AIMD calculations. The temperature is 3000 K.

CNs are the number of coordination atoms around the central atom of a compound. The RDFs depend on the multilayered coordination radius and coordination particle numbers. The CNs could be calculated by integration of the RDFs

$$N = 4\pi\rho \int_0^{R_{\min}} g_{\alpha\beta}(r)r^2 dr \quad (2)$$

where N is the CN. ρ is particle density in the simulation cell. R_{\min} is the first minimum in Figures 3a and 4a. As is shown in Figure 3b, we now concentrate on the CNs of Si_3N_4 . The results calculated by MD are compared with the AIMD simulation results. The CNs calculated by MD fit the AIMD results accurately, as well as in Figure 4b. The CNs are proportional to the pair distance and CNs are zero when the pair distance is less than 1.5 Å, so the minimal pair distance of Si_3N_4 is 1.5 Å. The BADs were calculated to analyze the local geometries of the first coordination shell, which can be calculated by

$$\theta_{ijk} = \left\langle \cos^{-1} \frac{r_{ij}^2 + r_{ik}^2 - r_{jk}^2}{2r_{ij}r_{ik}} \right\rangle \quad (3)$$

where θ is the bond angle. r_{ij} , r_{ik} , and r_{jk} are the bond length between atoms. The BADs of Si_3N_4 obtained by MD and AIMD at 2000 K and 3000 K are shown in Figures 5 and 6, respectively. At 2000 K, there are few BAD smaller than 45°. The majority of BADs are

localized between 75° and 120° , and the Si-N-Si and N-Si-N peak values of MD BADs are 90° , which is consistent with AIMD BADs. As for 3000 K, though the curves are rougher than that of 2000 K, the Si-N-Si and N-Si-N peak values of MD BADs are consistent well with AIMD BADs. Therefore, NNP is reliable enough to predict CNs and BADs information of SiN_x . Based on the RDFs, CNs, and BADs analysis above, it can be concluded that we can use the NNP to calculate the structure information of SiN_x .

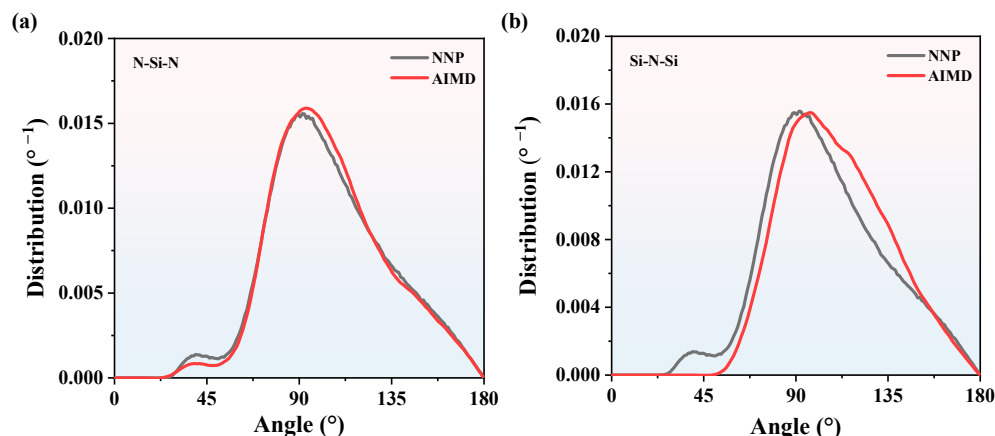


Figure 5. The BADs comparison of Si_3N_4 between NNP + MD and AIMD at 2000 K. (a) the N-Si-N BADs, (b) the Si-N-Si BADs.

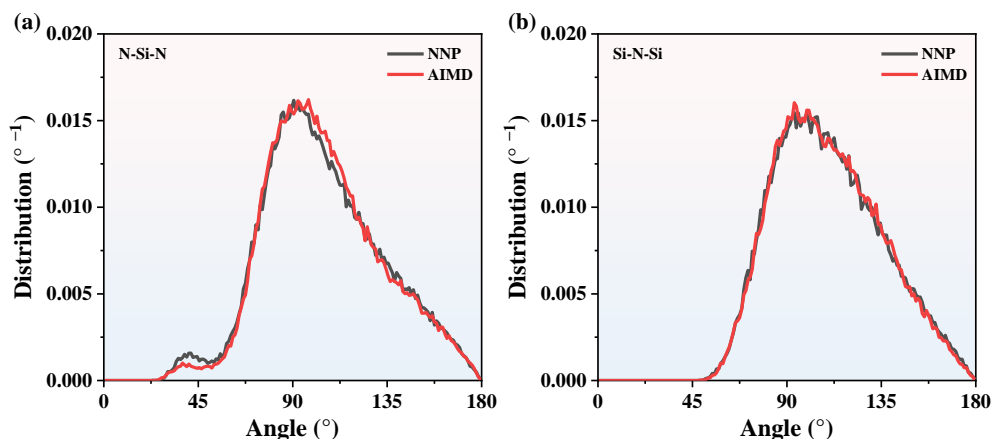


Figure 6. The BADs comparison of Si_3N_4 between NNP + MD and AIMD at 3000 K. (a) the N-Si-N BADs, (b) the Si-N-Si BADs.

3.2. The NPP Applied for Structure Information

Similar to the empirical potentials, the NNP can also be used for different compositions with the same elements. To study the effect of compositions on SiN_x structures, we used the NNP to simulate the heating process of SiN_x and analyzed the simulation results, including RDFs, CNs, and BADs. The models of SiN_x were built by LAMMPS, as shown in Figure 7. The parameters of SiN_x models are shown in Table 1. The boundary condition, timestep, ensemble, and other parameters of MD simulations are the same as part 3 for Si_3N_4 .

Table 1. The simulation parameters in SiN_x heating process.

Si:N	x (Å)	y (Å)	z (Å)	Atoms
4:5	54	54	54	13500
5:6	54	54	54	13750
6:7	54	54	54	14625
7:8	54	54	54	13125
1:1	54	54	54	13500

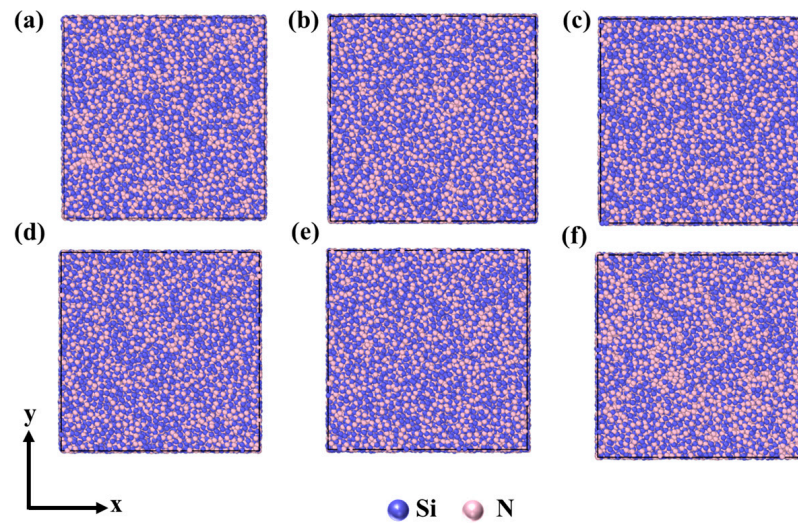


Figure 7. The models of SiN_x . (a) $x = 4/3$, (b) $x = 5/4$, (c) $x = 6/5$, (d) $x = 7/6$, (e) $x = 8/7$, (f) $x = 1/1$.

The RDFs of SiN_x at 2000 K and 3000 K are shown in Figure 8. In terms of a given temperature, the $g(r)$ peak values decrease while the proportion of Si composition increase, indicating that the pair distance decrease in SiN_x with a higher Si proportion. In the case of 2000 K, the peak and valley values fluctuate more obviously. As the temperature increases to 3000 K, there are few differences between the peak values of different compositions, indicating that all the SiN_x are in the same phase and there is less difference in microstructure as the temperature increases. The heating process for SiN_x was calculated as well with the RDFs at different temperatures shown in Figure S1.

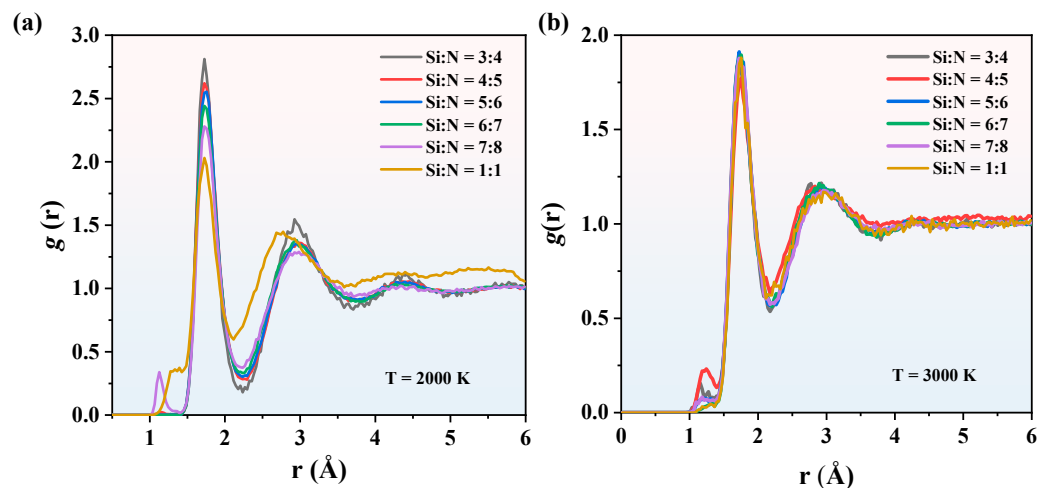


Figure 8. The RDFs of SiN_x at (a) 2000 K and (b) 3000 K.

During the heating process, CNs and BADs at 3000 K are shown in Figure 9. The CNs of SiN_x in Figure 9a share the same profile, which is all proportional to the pair distance. Among these CNs, SiN_x with a 3:4 composition, has the largest CN, which corresponds to the largest $g(r)$ in the Si-poor model. Therefore, Si_3N_4 is expected to deliver the most stable configuration at the micro level. With the increase of x in SiN_x , the CNs decrease slightly, indicating that the CNs are weakly affected by composition. The BADs of SiN_x at 3000 K are shown in Figure 9b,c. Similar to the CNs, the composition has little influence on the BADs, especially for the N-Si-N BADs in Figure 9c. In summary, the RDFs, CNs, and BADs of SiN_x are different, so the structures of SiN_x are different as well. In the next section, we used tensile simulations to explain the impact of different compositions on SiN_x mechanical properties from a macro perspective.

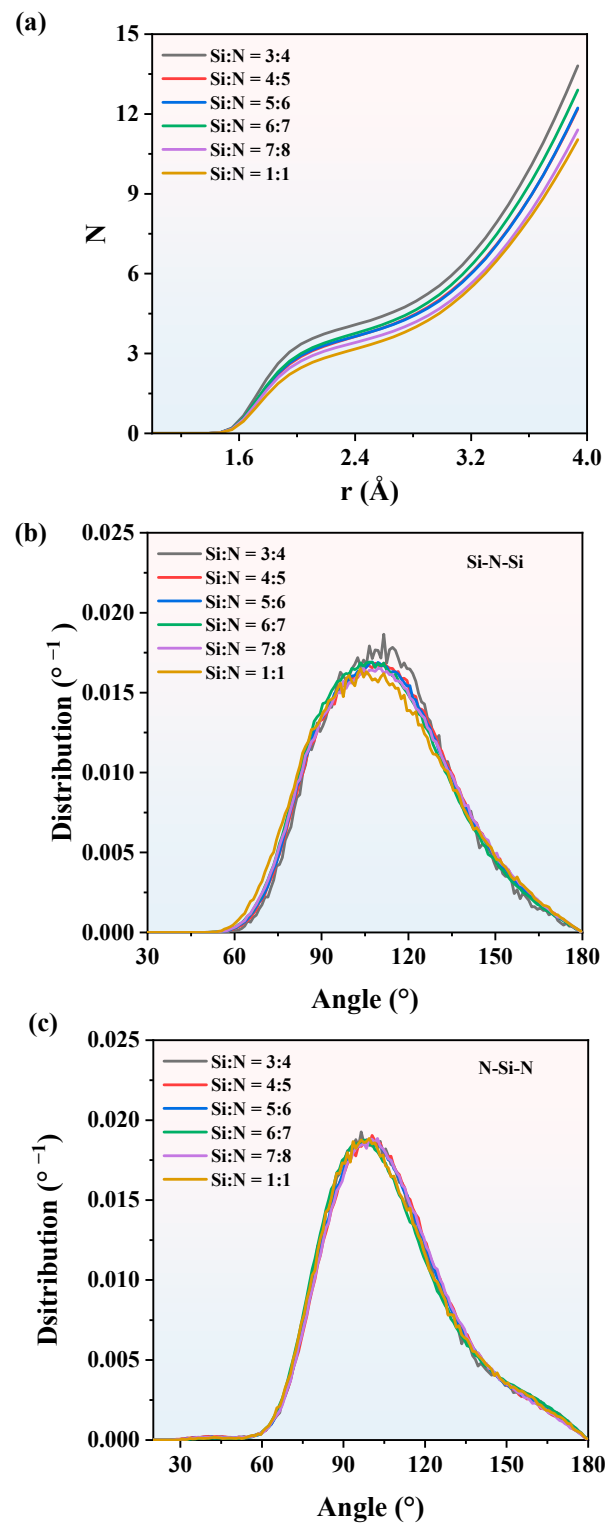


Figure 9. (a) The CNs of SiN_x at 3000 K. The BADs of (b) Si-N-Si and (c) N-Si-N at 3000 K.

3.3. The NNP Applied for Tensile Tests

To evaluate the accuracy of tensile by MD, the simulated strain–stress curve of Si₃N₄ compared with the experimental result is shown in Figure 10. The elastic modulus E of the simulation and experiment is 284.6 GPa and 253.3 GPa, respectively, which are consistent well with the reported E in the previous reference [38,39]. As is known, the E depends on the size of the model [39,40]; the simulated E 10.9% higher than the experimental case is

acceptable for the tensile test. It is impossible to fabricate the perfect single crystal Si_3N_4 in the experiment. The Si_3N_4 mechanical strength is determined by the defects and grain boundaries, so the experimental mechanical strength of Si_3N_4 is typically smaller than those of calculated results. The tensile tests of Si_3N_4 at different temperatures were calculated as well shown in Figure S2. The results show that the elastic modulus and peak values vary inversely with the temperature increasing, so when the temperature is 300 K, the mechanical properties of Si_3N_4 perform better than those at 1000 K and 3000 K. Since the accuracy of MD has been confirmed, the tensile tests of SiN_x with compositions from 3:4 to 1:1 were calculated at 300 K. The tensile models of SiN_x were repeated to supercells from the stable structures in part 4 with parameters of tensile models shown in Figure S3. The cross-sections of SiN_x in the tensile tests are shown in Figure 11. It can be seen that the cross-section of Si_3N_4 is flat, and the strain is small, so the Si_3N_4 cracked immediately and exhibited brittleness properties. In terms of other SiN_x , the lengths in the y direction are larger than that of Si_3N_4 when the fractures occurred, indicating that it takes a long time for the SiN_x to crack. With the increase of x , the SiN_x starts to exhibit flexibility, especially the SiN with the largest deformation when the fracture occurred.

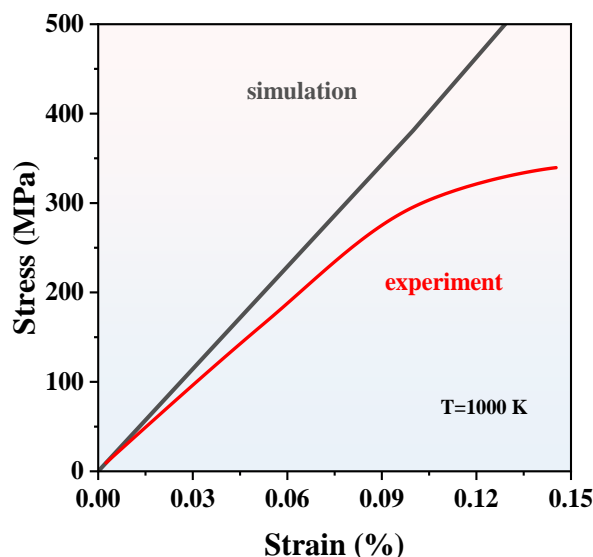


Figure 10. The simulated and experimental [39] strain–stress comparison of Si_3N_4 . Reproduced with permission [39]. Copyright 2018 Elsevier.

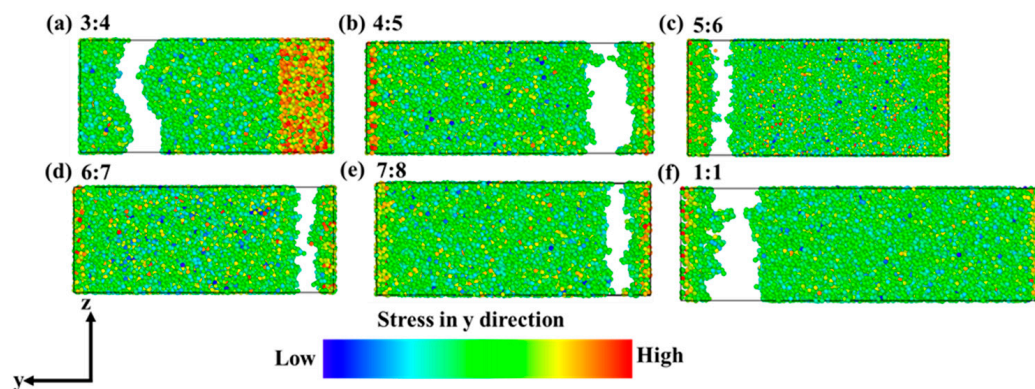


Figure 11. The cross-sections of SiN_x in the tensile tests. (a) $x = 4/3$, (b) $x = 5/4$, (c) $x = 6/5$, (d) $x = 7/6$, (e) $x = 8/7$, (f) $x = 1/1$.

The strain–stress curves and mechanical properties of SiN_x are shown in Figure 12. All the curves have a linear increase at the initial stage, which corresponds to an elastic deformation. The slopes of SiN_x at the initial linear stage are different, indicating that

the E varies with different compositions. The E is an important parameter of materials at the macro level, which represents the ability of an object to resist elastic deformation and reflects the bond strength between atoms, ions, or molecules at the micro level. The Si_3N_4 curve has a steep slope and large yield stress σ_s in the linear stage, illustrating that Si_3N_4 is a typical brittle material. On the contrary, another SiN_x demonstrates ductile property, especially the SiN with an obvious yield stage. When the strain ranges from 10% to 22%, the SiN curve becomes flat in the yield stage. The flexibility of SiN significantly improved compared with its Si_3N_4 counterpart, which is consistent with the analysis in Figure 8. The E of the maximal and minimal slope is 349.78 GPa and 138.39 GPa for $x = 4/3$ and $x = 1/1$, respectively. The E is 199.68 GPa, 188.95 GPa, 240.82 GPa, and 160.48 GPa, respectively, when $x = 5/4, 6/5, 7/6$, and $8/7$. Besides the E , the σ_s of SiN_x are different as well, showing that fracture occurs at different stages during the tensile simulations. The maximal σ_s is 27.45 GPa of Si_3N_4 . Although the σ_s of other SiN_x decrease with higher x , the σ_s of SiN_x fail to vary inversely with the x due to the amorphous structures of SiN_x ($x = 5/4, 6/5, 7/6$, and $8/7$). Among these curves, the 3:4 composition has the maximal E and σ_s , which can correspond to the largest RDFs and CNs in Figures 8 and 9, respectively. The RDFs and CNs decrease with the decreasing of x , leading to the flexibility improvement of SiN_x , since for Si_3N_4 $x = 4/3$ while for SiN $x = 1$. Meanwhile, the E of SiN_x excluding Si_3N_4 decrease compared with that of Si_3N_4 , which is generally inversely proportional to the RDFs. The results show that the RDFs and CNs at the micro level can reflect the macro mechanical properties of SiN_x to a large extent.

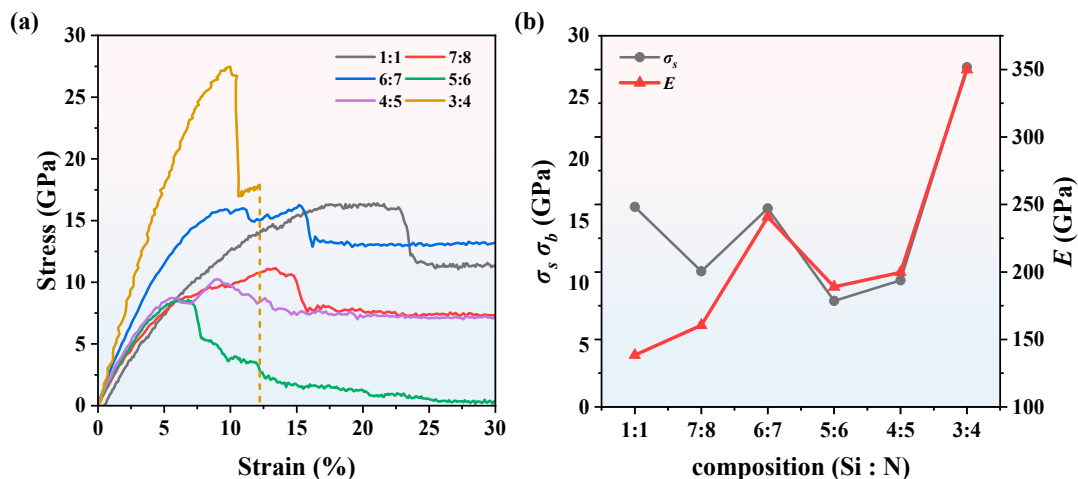


Figure 12. (a) The strain–stress curves of SiN_x at 300 K. (b) The mechanical properties of SiN_x .

4. Conclusions

In this work, the interatom potential for SiN_x was created by the DEEPM kit with a neural network. Based on the comparison of energies and forces from NNP and AIMD for $\text{trans-Si}_3\text{N}_4$, we find that NNP can easily achieve DFT accuracy. The RDFs, CNs, and BADs simulations between the NNP and AIMD confirmed that the NNP is reliable enough to calculate the structure information Si_3N_4 as well. Then, we conducted comprehensive calculations to predict the RDFs, CNs, and BADs of SiN_x . Therefore, we used tensile simulations to explain the impact of different compositions on SiN_x properties from a macro perspective. Si_3N_4 is a typical brittle material with the largest E and σ_s . The flexibility of SiN_x , excluding Si_3N_4 , improved, leading to the decrease of E and σ_s . The E and σ_s fail to be inversely proportional with x due to the amorphous structures of SiN_x . The RDFs and CNs at the micro level can reflect the macro mechanical properties of SiN_x to a large extent. Among these compositions, $x = 4/3$ features high mechanical strength, owing to the largest CN and RDF. The E of SiN_x , excluding Si_3N_4 , decreases compared with that of Si_3N_4 , leading to the flexibility improvement of SiN_x , which is generally inversely proportional to the RDFs.

Supplementary Materials: The following supporting information can be downloaded at: <https://www.mdpi.com/article/10.3390/nano13081352/s1>, Figure S1: The RDFs of SiN_x with different compositions in heating process; Figure S2: Amorphous Si₃N₄ tensile simulations; Figure S3: The whole process of fracture during tensile simulations; Table S1: The specific simulation parameters in SiN_x tensile simulations.

Author Contributions: Conceptualization, H.X. and Z.L.; methodology, H.X. and Z.L.; formal analysis, H.X. and Z.L.; data curation, H.X., Z.L. and Y.G.; writing—original draft preparation, H.X.; writing—review and editing, H.X., Z.L., S.S., Y.G., Z.Z. and S.L.; project administration, Y.G.; funding acquisition, Y.G. and S.L. All authors have read and agreed to the published version of the manuscript.

Funding: This work is supported by Wuhan University. The authors acknowledge the financial support from the National Natural Science Foundation of China (Grant Nos. 62174122, U2241244, 51727901). The numerical calculations in this work were conducted on the supercomputing system in the Supercomputing Center of Wuhan University.

Data Availability Statement: The data that support the findings of this study are available from the corresponding author upon reasonable request.

Conflicts of Interest: The authors declare that they have no known competing financial interests or personal relationships that could have appeared to influence the work reported in this paper.

References

1. Car, R.; Parrinello, M. Unified approach for molecular dynamics and density-functional theory. *Phys. Rev. Lett.* **1985**, *55*, 2471–2474. [[CrossRef](#)]
2. Bergstra, J.A.; Bethke, I. Molecular dynamics. *J. Logic. Algebr. Program.* **2002**, *51*, 193–214. [[CrossRef](#)]
3. Geerlings, P.; Boon, G.; Van Alsenoy, C.; De Proft, F. Density functional theory and quantum similarity. *Int. J. Quantum Chem.* **2005**, *101*, 722–732. [[CrossRef](#)]
4. Morgon, N.H.; Custodio, R. The density-functional theory. *Quim. Nova.* **1995**, *18*, 44–55.
5. Sandre, E.; Pasturel, A. An introduction to ab-initio molecular dynamics schemes. *Mol. Simul.* **1997**, *20*, 63–77. [[CrossRef](#)]
6. Verlet, L. Computer “experiments” on classical fluids. I. thermodynamical properties of Lennard-Jones molecules. *Phys. Rev.* **1967**, *159*, 98. [[CrossRef](#)]
7. Finnis, M.; Sinclair, J. A simple empirical N-body potential for transition metals. *Philos. Mag. A* **1984**, *50*, 45–55. [[CrossRef](#)]
8. Daw, M.S.; Baskes, M.I. Embedded-atom method: Derivation and application to impurities, surfaces, and other defects in metals. *Phys. Rev. B* **1984**, *29*, 6443. [[CrossRef](#)]
9. Vink, R.; Barkema, G.; Van der Weg, W.; Mousseau, N. Fitting the Stillinger–Weber potential to amorphous silicon. *J. Non-Cryst. Solids.* **2001**, *282*, 248–255. [[CrossRef](#)]
10. Hossain, M.; Hao, T.; Silverman, B. Stillinger–Weber potential for elastic and fracture properties in graphene and carbon nanotubes. *J. Phys. Condens. Matter.* **2018**, *30*, 055901. [[CrossRef](#)]
11. Tersoff, J. New empirical approach for the structure and energy of covalent systems. *Phys. Rev. B* **1988**, *37*, 6991. [[CrossRef](#)] [[PubMed](#)]
12. Liang, T.; Shan, T.-R.; Cheng, Y.-T.; Devine, B.D.; Noordhoek, M.; Li, Y.; Lu, Z.; Phillpot, S.R.; Sinnott, S.B. Classical atomistic simulations of surfaces and heterogeneous interfaces with the charge-optimized many body (COMB) potentials. *Mater. Sci. Eng. R Rep.* **2013**, *74*, 255–279. [[CrossRef](#)]
13. De Tomas, C.; Suarez-Martinez, I.; Marks, N.A. Graphitization of amorphous carbons: A comparative study of interatomic potentials. *Carbon* **2016**, *109*, 681–693. [[CrossRef](#)]
14. Deringer, V.L.; Csányi, G. Machine learning based interatomic potential for amorphous carbon. *Phys. Rev. B* **2017**, *95*, 094203. [[CrossRef](#)]
15. Rowe, P.; Csányi, G.; Alfè, D.; Michaelides, A. Development of a machine learning potential for graphene. *Phys. Rev. B* **2018**, *97*, 054303. [[CrossRef](#)]
16. Behler, J.; Parrinello, M. Generalized neural-network representation of high-dimensional potential-energy surfaces. *Phys. Rev. Lett.* **2007**, *98*, 146401. [[CrossRef](#)] [[PubMed](#)]
17. Zhang, L.; Han, J.; Wang, H.; Car, R.; Weinan, E. Deep potential molecular dynamics: A scalable model with the accuracy of quantum mechanics. *Phys. Rev. Lett.* **2018**, *120*, 143001. [[CrossRef](#)] [[PubMed](#)]
18. Bonati, L.; Parrinello, M. Silicon liquid structure and crystal nucleation from ab-initio deep metadynamics. *Phys. Rev. Lett.* **2018**, *121*, 265701. [[CrossRef](#)]
19. Wen, T.; Wang, C.-Z.; Kramer, M.; Sun, Y.; Ye, B.; Wang, H.; Liu, X.; Zhang, C.; Zhang, F.; Ho, K.-M. Development of a deep machine learning interatomic potential for metalloid-containing Pd-Si compounds. *Phys. Rev. B* **2019**, *100*, 174101. [[CrossRef](#)]
20. Xu, N.; Shi, Y.; He, Y.; Shao, Q. A deep-learning potential for crystalline and amorphous Li-Si alloys. *J. Phys. Chem. C* **2020**, *124*, 16278–16288. [[CrossRef](#)]

21. Gritsenko, V.A. Electronic structure of silicon nitride. *Physics-Usppekhi* **2012**, *55*, 498–507. [[CrossRef](#)]
22. Kaloyeros, A.E.; Pan, Y.L.; Goff, J.; Arkles, B. Review-silicon nitride and silicon nitride-rich thin film technologies: State-of-the-art processing technologies, properties, and applications. *ECS J. Solid State Sci. Technol.* **2020**, *9*. [[CrossRef](#)]
23. Popper, P. Applications of Silicon-Nitride. In *Silicon Nitride 93*; Hoffmann, M.J., Becher, P.F., Petzow, G., Eds.; Trans Tech Publications: Clausthal Zellerfe, 1994; Volumes 89–91, pp. 719–723.
24. Li, L.Q.; Wang, S.F.; Ovcharenko, A.; Wang, W.Y. Molecular Dynamics Study of Nano-Tribological Properties of Silicon Nitride Films. In Proceedings of the ASME Design Engineering Technical Conferences and Computers and Information in Engineering Conference (DETC), Buffalo, NY, USA, 17–20 August 2014.
25. Rettore, R.P.; Brito, M.A.M. Mechanical properties of silicon-nitride bonded silicon-carbide refractory and its relation microstructure. In *Silicon Nitride 93*; Hoffmann, M.J., Becher, P.F., Petzow, G., Eds.; Trans Tech Publications: Clausthal Zellerfe, 1994; Volumes 89–91, pp. 553–557.
26. Wiederhorn, S.M.; Quinn, G.D.; Krause, R. High-temperature structural reliability of silicon-nitride. In *Silicon Nitride 93*; Hoffmann, M.J., Becher, P.F., Petzow, G., Eds.; Trans Tech Publications: Clausthal Zellerfe, 1994; Volumes 89–91, pp. 575–580.
27. Gismatulin, A.A.; Gritsenko, V.A.; Yen, T.J.; Chin, A. Charge transport mechanism in SiN_x-based memristor. *Appl. Phys. Lett.* **2019**, *115*, 253502. [[CrossRef](#)]
28. Gismatulin, A.A.; Kamaev, G.N.; Kruchinin, V.N.; Gritsenko, V.A.; Orlov, O.M.; Chin, A. Charge transport mechanism in the forming-free memristor based on silicon nitride. *Sci. Rep.* **2021**, *11*. [[CrossRef](#)] [[PubMed](#)]
29. Gritsenko, V.A.; Gismatulin, A.A.; Baraban, A.P.; Chin, A. Mechanism of stress induced leakage current in Si₃N₄. *Mater. Res. Express.* **2019**, *6*, 076401. [[CrossRef](#)]
30. Gritsenko, V.A.; Gismatulin, A.A.; Chin, A. Multiphonon trap ionization transport in nonstoichiometric SiN_x. *Mater. Res. Express.* **2019**, *6*, 036304. [[CrossRef](#)]
31. Sun, C.; Liu, A.Y.; Samadi, A.; Chan, C.; Ciesla, A.; Macdonald, D. Transition metals in a cast-monocrystalline silicon ingot studied by silicon nitride gettering. *Phys. Status Solidi-R.* **2019**, *13*. [[CrossRef](#)]
32. Liu, A.Y.; Sun, C.; Sio, H.C.; Zhang, X.Y.; Jin, H.; Macdonald, D. Gettering of transition metals in high-performance multicrystalline silicon by silicon nitride films and phosphorus diffusion. *J. Appl. Phys.* **2019**, *125*. [[CrossRef](#)]
33. Wang, H.; Zhang, L.; Han, J.; Weinan, E. DeePMD-kit: A deep learning package for many-body potential energy representation and molecular dynamics. *Comput. Phys. Commun.* **2018**, *228*, 178–184. [[CrossRef](#)]
34. Kresse, G.; Furthmüller, J. Efficient iterative schemes for ab initio total-energy calculations using a plane-wave basis set. *Phys. Rev. B* **1996**, *54*, 11169. [[CrossRef](#)]
35. Perdew, J.P.; Burke, K.; Ernzerhof, M. Generalized gradient approximation made simple. *Phys. Rev. Lett.* **1996**, *77*, 3865. [[CrossRef](#)] [[PubMed](#)]
36. Plimpton, S. Fast parallel algorithms for short-range molecular dynamics. *J. Comput. Phys.* **1995**, *117*, 1–19. [[CrossRef](#)]
37. Peng, Y.; Wang, S.F.; Zhang, Y.; Gao, Y.N. Simulation and application of molecular dynamics in materials science. *Adv. Mater. Res.* **2012**, *572*, 232–236. [[CrossRef](#)]
38. Kossowsky, R.; Miller, D.G.; Diaz, E.S. Tensile and creep strengths of hot-pressed Si₃N₄. *J. Mater. Sci.* **1975**, *10*, 983–997. [[CrossRef](#)]
39. Yao, D.X.; Chen, H.B.; Zuo, K.H.; Xia, Y.F.; Yin, J.W.; Liang, H.Q.; Zeng, Y.P. High temperature mechanical properties of porous Si₃N₄ prepared via SRBSN. *Ceram. Int.* **2018**, *44*, 11966–11971. [[CrossRef](#)]
40. Nakajima, H.; Chang, T.F.M.; Chen, C.Y.; Konishi, T.; Machida, K.; Toshiyoshi, H.; Yamane, D.; Masu, K.; Sone, M. A Study on Young's Modulus of Electroplated Gold Cantilevers for MEMS Devices. In Proceedings of the 12th IEEE Annual International Conference on Nano/Micro Engineered and Molecular Systems (IEEE-NEMS), Los Angeles, CA, USA, 9–12 April 2017; pp. 264–267.

Disclaimer/Publisher's Note: The statements, opinions and data contained in all publications are solely those of the individual author(s) and contributor(s) and not of MDPI and/or the editor(s). MDPI and/or the editor(s) disclaim responsibility for any injury to people or property resulting from any ideas, methods, instructions or products referred to in the content.